

## First Image of the Sun with MeerKAT Solar Observations: Opening a New Frontier in Solar Physics

DEVOJYOTI KANSABANIK <sup>1</sup>, SURAJIT MONDAL <sup>2</sup>, DIVYA OBEROI <sup>1</sup>, JAMES O. CHIBUEZE <sup>3,4,5</sup>, N. E. ENGELBRECHT,<sup>4</sup>  
R. D. STRAUSS,<sup>4</sup> E. P. KONTAR <sup>6</sup>, G. J. J. BOTHA,<sup>7</sup> AND RUHANN STEYN<sup>4</sup>

<sup>1</sup>*National Centre for Radio Astrophysics, Tata Institute of Fundamental Research, S. P. Pune University Campus, Pune 411007, India*

<sup>2</sup>*Center for Solar-Terrestrial Research, New Jersey Institute of Technology, 323 M L King Jr Boulevard, Newark, NJ 07102-1982, USA*

<sup>3</sup>*Department of Mathematical Sciences, University of South Africa, Cnr Christian de Wet Rd and Pioneer Avenue, Florida Park, 1709, Roodepoort, South Africa*

<sup>4</sup>*Centre for Space Research, Physics Department, North-West University, Potchefstroom 2520, South Africa*

<sup>5</sup>*Department of Physics and Astronomy, Faculty of Physical Sciences, University of Nigeria, Carver Building, 1 University Road, Nsukka 410001, Nigeria*

<sup>6</sup>*School of Physics and Astronomy, University of Glasgow, Glasgow, G12 8QQ, UK*

<sup>7</sup>*Department of Mathematics, Physics and Electrical Engineering, Northumbria University, Newcastle upon Tyne, NE1 8ST, UK*

### ABSTRACT

Solar radio emissions provide several unique diagnostics to estimate different physical parameters of the solar corona, which are otherwise simply inaccessible. However, imaging the highly dynamic solar coronal emissions spanning a large range of angular scales at radio wavelengths is extremely challenging. At GHz frequencies, the MeerKAT radio telescope is possibly globally the best-suited instrument at the present time and can provide high-fidelity spectroscopic snapshot solar images. Here, we present the first images of the Sun made using the observations with the MeerKAT at L-band (856 – 1711 MHz). This work demonstrates the high fidelity of the MeerKAT solar images through a comparison with simulated radio images at the MeerKAT frequencies. The observed images show extremely good morphological similarities with the simulated images. A detailed comparison between the simulated radio map and observed MeerKAT radio images demonstrates that there is significant missing flux density in MeerKAT images at the higher frequencies of the observing band, though it can potentially be estimated and corrected for. We believe once solar observations with the MeerKAT are commissioned, they will not only enable a host of novel studies but also open the door to a large unexplored phase space with significant discovery potential.

*Keywords:* Radio interferometers(1345) – Solar radio emission(1522) – Solar radio telescopes(1523) – Solar instruments(1499) – Solar coronal radio emission(1993) – Solar corona(1483)

### 1. INTRODUCTION

Since the discovery of solar radio emission (Reber 1944), the Sun has been studied in great detail in a wide range of frequencies spanning from a few kHz to several hundreds of GHz. Despite this long history of observations and studies, the Sun still harbors several mysteries. With each leap of technological advancement in building new telescopes, several of these mysteries are solved. At the same time, these new advancements probe the Sun in a very new light and hence generally open up a very rich discovery space. Interesting results coming from new instruments like the Solar orbiter (Müller, D. et al. 2020; García Marirrodriga, C. et al. 2021), Parker Solar Probe (Raouafi et al. 2023), Daniel K. Inouye Solar Telescope

(DKIST, Rimmele et al. 2020; Rast et al. 2021), Murchison Widefield Array (MWA, Lonsdale et al. 2009; Tingay et al. 2013; Wayth et al. 2018), LOw Frequency ARray (LOFAR, van Haarlem et al. 2013), Expanded Owens Valley Solar Array (EOVSA, Gary et al. 2012), the NenuFAR (Zarka et al. 2018; Briand et al. 2022), the Owens Valley Long Wavelength Array (OVRO-LWA; Hallinan et al. 2023) are testament to this. Most of these new-generation radio telescopes are not dedicated to solar observations (except EOVSA), but these are the ones that are expected to open up large expanses of pristine phase space unexplored yet. The MeerKAT (Jonas & MeerKAT Team 2016; Chen et al. 2021) is another such new generation radio interferometric array, which can

open a new frontier in solar radio physics at GHz frequencies.

MeerKAT, originally known as the Karoo Array Telescope, is a new-generation radio telescope located in the MeerKAT National Park in the Northern Cape of South Africa. It consists of 64 dishes, each with a diameter of 13.5 m. Each dish is equipped with a cryogenically cooled receiver, making it extremely sensitive. At present, MeerKAT has three observing bands – UHF (544–1087 MHz), L (856–1711 MHz), and S (1750–3499 MHz) bands. The array is centrally condensed with about 39 dishes lying within 1 km and the remaining dishes distributed within a radius of  $\sim 8$  km. This provides MeerKAT with extremely good surface brightness sensitivity and also allows the generation of radio images with extremely high dynamic range and image fidelity (e.g. Heywood et al. 2022). The dense array layout of MeerKAT also implies that it has an excellent spectroscopic snapshot sampling in Fourier plane ( $uv$ -plane) as shown in Figure 1. This provides a very well-behaved point-spread-function (PSF) of the MeerKAT array and makes it well-suited for high dynamic range (DR) spectroscopic snapshot imaging. This capability is extremely useful for solar studies at radio wavelengths due to the fast dynamics seen in solar radio emissions both in the spectral and temporal domain (Mondal et al. 2019; Kansabanik 2022). There are several avenues where high dynamic range snapshot imaging can lead to extraordinary science ranging from the direct estimation of the magnetic field of the coronal mass ejections (CMEs) close to the Sun to studies of nonthermal emission from extremely weak radio transients.

Here we present the first imaging observation of the Sun with the MeerKAT. Unlike standard astronomical observations, solar observations with any radio telescope pose several challenges. These challenges need to be addressed before MeerKAT can be used for solar observations. The primary reason behind this is that MeerKAT was designed for observing faint astronomical sources. To observe the Sun, the source with the highest flux density in the sky, strong attenuators need to be used to ensure that the astronomical signal stays in the linear regime of the instrument. However, these same attenuators cannot be used to observe the available calibrators as these sources are orders of magnitude weaker than the Sun. In the absence of these calibrator observations, it is hard to estimate the instrumental gains and efforts that are ongoing toward solving these issues. Here we use a different technique to observe and image the Sun. Instead of pointing at the Sun, we pointed  $\sim 2.5^\circ$  away to keep it in the sidelobes of the primary beam to attenuate the solar emissions. The sensitivity of the MeerKAT

is sufficient to image the Sun even when it is in the sidelobes of the primary beam. Availability of holographic measurements of the MeerKAT primary beam up to the second side lobe (de Villiers & Cotton 2022; de Villiers 2023) allows us to obtain flux density calibrated solar images. We note that there are some shortcomings of this observing strategy. Among them, the chromatic nature of the primary beam makes the sensitivity over the solar disc non-uniform. Despite these shortcomings our work substantiates the excellent imaging quality of the MeerKAT solar data and showcase its potential for enabling excellent solar science.

This paper is organized as follows. Section 2 presents the details of the observations. Section 3 describes the data analysis procedure, including calibration, imaging, and primary beam correction. In Section 4, we present our results and demonstrate some early results we achieved using these data. Finally, in Section 5, we conclude by giving a future outlook of the MeerKAT solar observation.

## 2. OBSERVATIONS

These observations were done as a Director’s Discretion Time (DDT) and *Science Verification* (SSV) observation under project ID SSV-20200709-SA-01. Raw visibilities are already available in the public domain through SARAO data archive<sup>1</sup>. The observations were carried out during the 6th perihelion passage of Parker Solar Probe (PSP, Fox 2017) from 2020 September 24 to 2020 September 30. On each day, there are about 3 hours of observations centered around 10:30 UTC. In this paper, we present results from two of these epochs – 2020, September 26, and 2020 September 27.

Observations were done covering 856–1711 MHz with 32 K spectral channels and 8 s temporal resolution. This provides us with data at about 26 kHz spectral resolution. Standard MeerKAT flux density calibrator, J0408-6545, was observed at the start of observation. J0408-6545 is used for bandpass and flux density calibration (hereafter referred to as fluxcal). J1239-1023 is used as a phase calibrator (hereafter referred to as phasecal) and observed between each consecutive solar scan. Since the Sun is a non-sidereal source, its RA–DEC changes with time. Hence, the pointing center is changed every 15 minutes. For all the pointings, the Sun is kept at  $\sim 2.5^\circ$  away from the pointing center. The position of the Sun on the primary beam for different scans is shown for three different frequencies in Figure 2. It turns out that at the lower part of the band, the Sun is in the first side

<sup>1</sup> <https://archive.sarao.ac.za/>

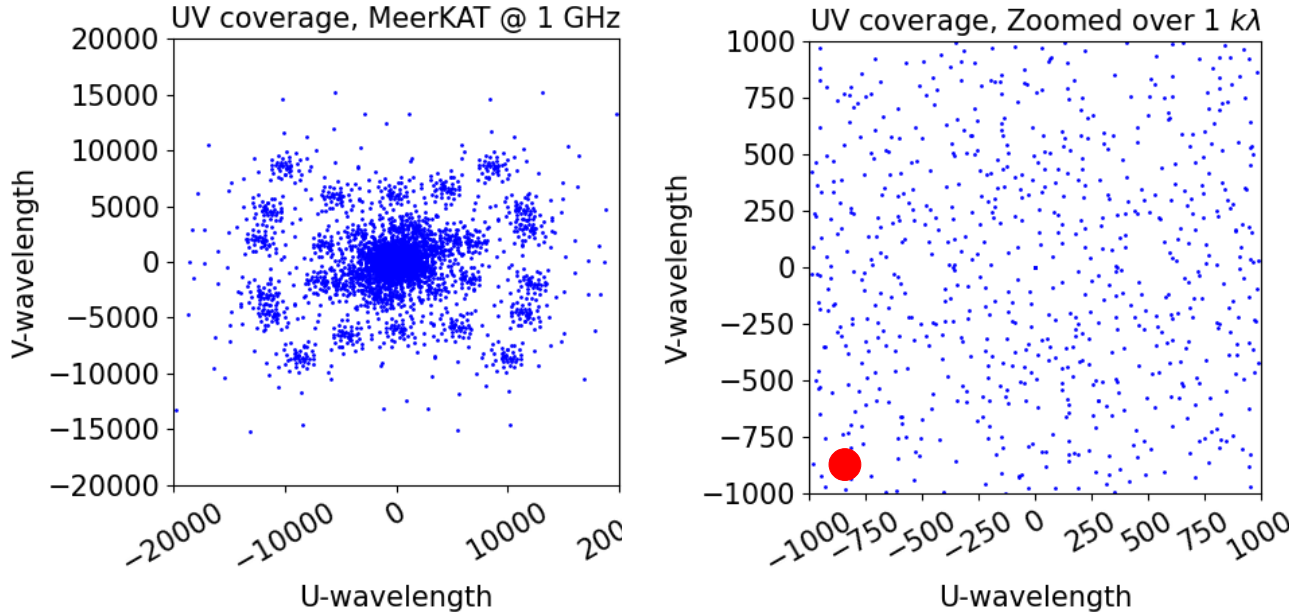


**Figure 1. MeerKAT spectroscopic snapshot  $uv$ -coverage.** **Left panel:** Snapshot  $uv$ -coverage of the MeerKAT at 1 GHz. **Right panel:** Same  $uv$ -coverage but zoomed in over  $1k\lambda$  central region. Red circle at the bottom left corner correspond to the  $uv$ -cell for a source with the size of solar disc of 32 arcmin in angular scale.

lobe of the primary beam, while it lies in the second side lobes or null at the higher parts of the band. This essentially makes the observations at the lower part more sensitive than the high parts of the band. Observing the Sun keeping it at the sidelobes provide about  $-50$  to  $-90$  dB attenuation, depending on the frequency, to the total solar power, which is essential to keep the signal in the linear regime all through the signal chain.

### 3. DATA ANALYSIS

Since the observation does not fall under the standard astronomical observation category, we did not use SRAO Science Data Processor (SDP) pipelines for the analysis. Instead, we did the analysis manually using Common Astronomy Software Application (CASA) (McMullin et al. 2007; The CASA Team et al. 2022) for flagging and calibration and WSClean (Offringa et al. 2014) for imaging.

#### 3.1. Flagging and Calibration

The flowchart of flagging and initial calibration procedures are shown in Figure 3. Initial flagging is performed to remove bad antennas, bad channels, and other strong radio frequency interferences (RFIs). After that, initial calibration rounds are done using the fluxcal and phasecal. A total of five rounds of initial calibration were done, each followed by post-calibration flagging steps. Detailed procedures for flagging and initial calibration are discussed in Appendix A and B, respectively.

Once initial calibration is done, calibration solutions are applied to the solar scans, and self-calibration is performed. The Sun is present in the sidelobes of the MeerKAT primary beam. Due to the chromatic nature of the primary beam, sensitivity across the solar disc varies with frequency. On the other hand, the Sun is a non-sidereal source. So, the position of the Sun in the equatorial coordinate system changes with time. Hence, we first moved the phasecenter of the measured visibilities to the solar center and then performed self-calibration for each 20 MHz spectral and 15-minute temporal chunk separately. Improvements in DR of the images with self-calibration iterations are shown in Figure 4. A detailed description of the self-calibration procedure followed here is presented in Appendix C.

#### 3.2. Final Imaging and Primary Beam Correction

**Fig. Set 1. Images of the Sun centered at 2020 September 27, 10:45 UTC.**

Once the self-calibration is done, we make final images of the Sun for each spectro-temporal chunk separately. For the final imaging, we used all baselines. All other imaging parameters – the number of  $w$ -layers, visibility weighting,  $uv$ -taper, multiscale parameters, and pixel size are kept the same. During the final imaging, we did not use any pre-defined mask. Instead, we use auto-masking parameter available in WSClean to perform deconvolution down to  $3\sigma$ , where  $\sigma$  is the rms calculated close to the Sun. Due to the chromatic nature of the primary beam, the low-frequency part of the band has

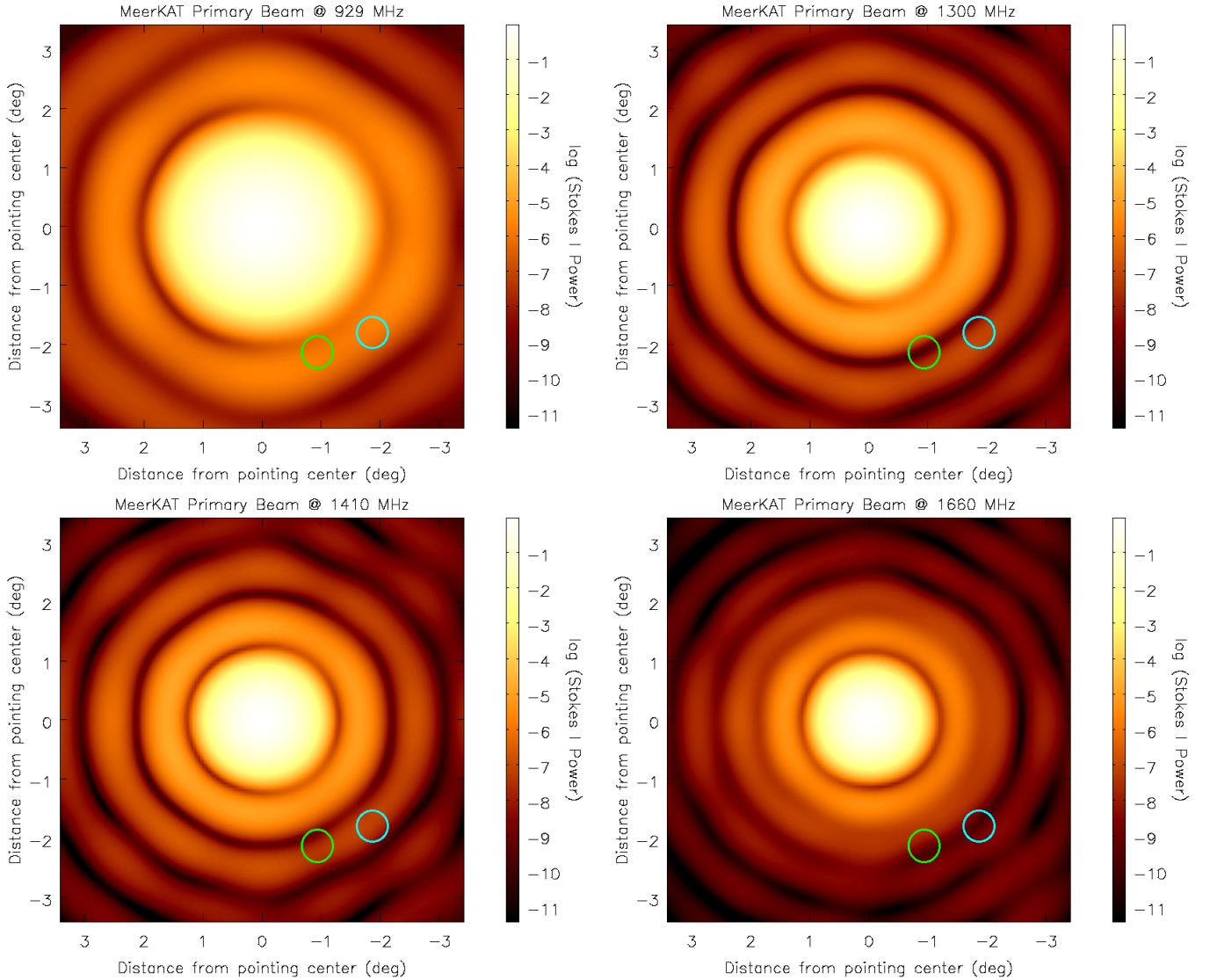


**Figure 2. Locations of the Sun with respect to the primary beam.** Four different panels show the MeerKAT holographic measured primary beam (de Villiers & Cotton 2022; de Villiers 2023). Cyan circle represent the location of the Sun on 2020 September 26 and green circle represent the location of the Sun on 2020 September 27 for a particle observing scan. The position of the Sun changed azimuthally with different scans, but lies in the similar distances from the center of the primary beam.

better sensitivity compared to the high-frequency part. This is evident from the spectral images shown in the bottom panels of Figure 5 and 3.2. At high frequencies, emissions from the active region bright points are detected with good detection significance, but the extended emission from solar limbs are not detected at all frequency chunks. To image all the structures detected across the full band, we have convolved all images at the resolution at the lowest frequency of the observing band. Then we normalized each 20 MHz spectral image with respect to the peak flux and stacked all spectral chunks for a given scan to obtain a full band image shown in the top panel of Figure 5 and 3.2.

Since the Sun is present at the sidelobes of the MeerKAT primary beam, we have to correct the primary beam response across the solar disc to obtain the correct flux density. Holographic measurements of the MeerKAT primary beam (de Villiers & Cotton 2022; de Villiers 2023) at L-band is available<sup>2</sup> over the extend of 4 degrees at an angular resolution of  $\sim 223$  arcsec. We did linear interpolation to obtain the beam values at each pixel of the image. For alt-az mount telescopes, the sky rotates with respect to the telescope beam, and this rotation is denoted by parallactic angle. If the beam

<sup>2</sup> MeerKAT holographic measurements of the primary beam.

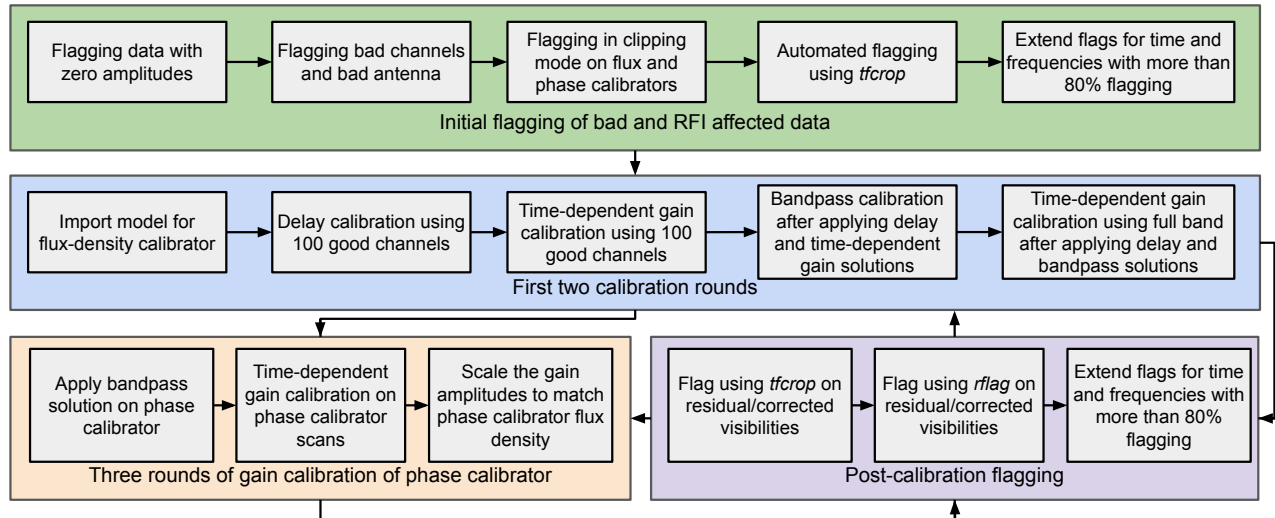


**Figure 3. Flowchart describing the flagging and initial calibration procedure.** Green box shows the steps of initial flagging on flux and phase calibrators. Blue box shows the first two rounds of calibration steps on the flux density calibrator. Each calibration round is followed by post-calibration flagging steps shown in the purple box. Orange box shows the steps of final three rounds of calibration on the phase calibrator.

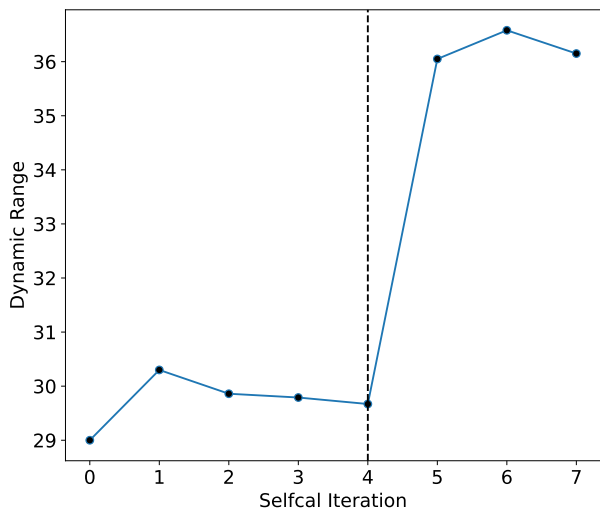


**Figure 4. Changes in the imaging dynamic range with self-calibration iterations** The black dotted line shows the iteration where amplitude-phase self-calibration is initiated.

of the instrument is axially symmetric, then parallactic angle correction is not important for Stokes I imaging. As evident from Figure 2, while the main lobe of the MeerKAT primary beam is close to axially symmetric, that is not true for its sidelobes. In the present observation, the Sun is present on the sidelobes of the primary beam. Hence, we performed parallactic angle correction to the primary beam before performing the primary beam correction. We have done image plane primary beam correction using the array-averaged response. Be-

ing at the first/second side lobe of the primary beam, flux density measurements can have errors due to primary beam measurements. Considering different kinds of errors as discussed in de Villiers (2023), we consider a conservative 10% error on the measured flux density.

#### 4. RESULTS

In this section we present the results from first MeerKAT solar observations and compare it with simulated MeerKAT solar maps at frequencies spanning our L-band observations.

##### 4.1. First Solar Image using MeerKAT

The first images of the Sun made using MeerKAT L-band observations are shown in Figures 5 and 6. The top panel shows the average image over the entire MeerKAT L-band and the lower panels show images at individual 20 MHz bands spanning the full observing band. The entire solar disc is clearly visible once images over the full band are stacked together. We find that the solar disc is about 35 arcmin in diameter, slightly larger than the optical disc. MeerKAT images are overlaid on 193Å images from the Atmospheric Imaging Assembly (AIA) onboard Solar Dynamics Observatory (SDO; Lemen et al. 2012) in Figure 6. The largest active region is co-located with the brightest radio source in the MeerKAT images. There are multiple small active region bright points visible in AIA image, which are also detected in MeerKAT images with high significance. In both of these images, the diffuse quiet Sun emission from both the limbs is also detected with good significance. Although, visually both the images show features sim-

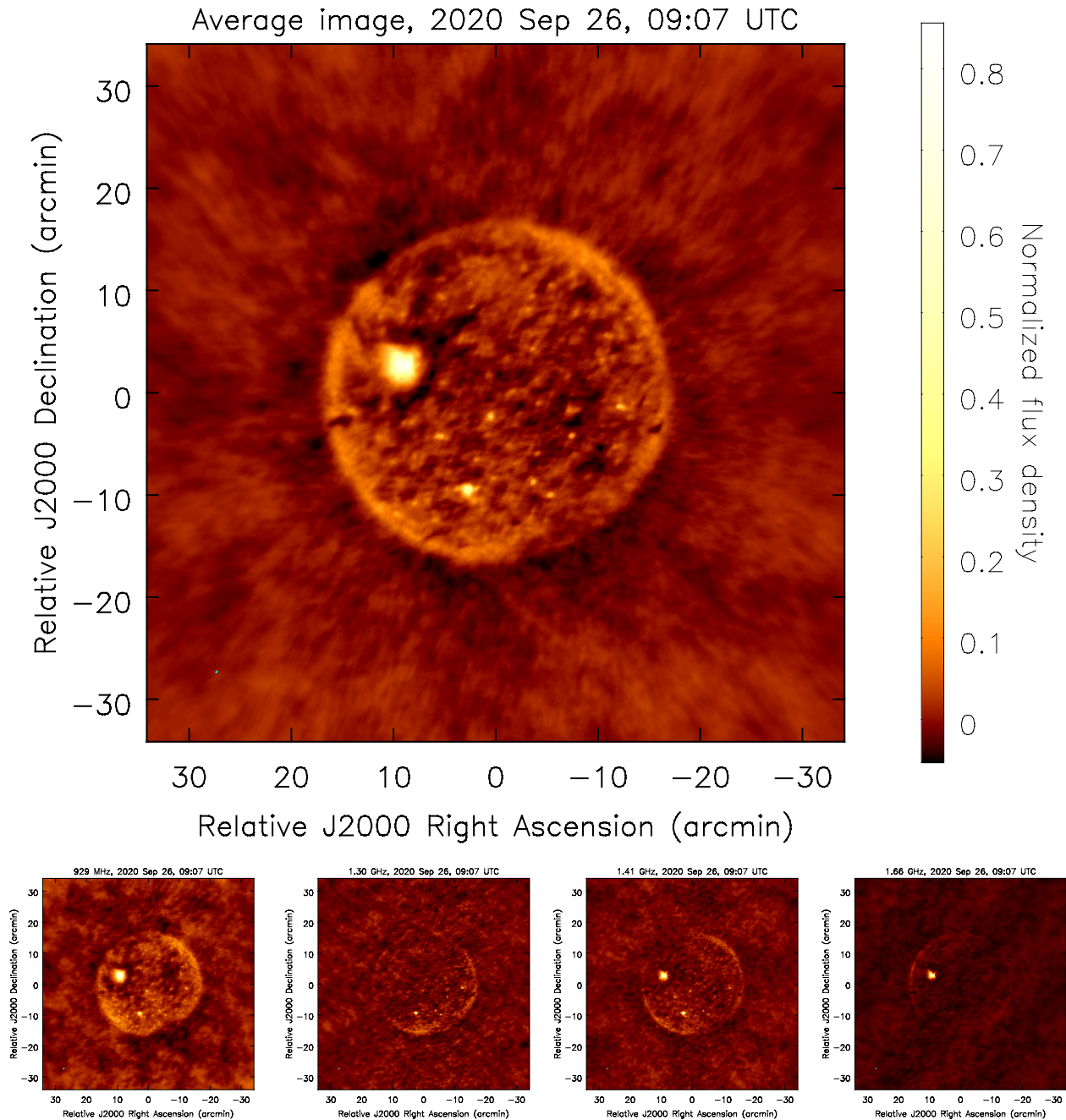


**Figure 5.** First image of the Sun on 2020 September 26, 09:07 UTC. **Top panel:** Normalized average image over the entire MeerKAT L-band. **Bottom panels:** Images at different 20 MHz spectral chunks across the observing band. The small cyan dot at the bottom left is the point-spread-function of the array.

ilar to those seen in the AIA images, we go further to verify this via comparison with corresponding simulated solar radio images.

#### 4.2. Simulating Solar Radio Images and Spectra

The simulated images only aim to capture the free-free thermal emission. To generate simulated images, a differential emission measure (DEM) inversion using images at different wavelengths from the AIA/SDO is

performed. To reduce the computation time and improve the signal-to-noise of the obtained DEMs, the AIA images were smoothed to a resolution of 4.8 arcsec, before DEM inversion. Note, though that the resolution of these smoothed images is still higher than those of the MeerKAT radio images. Following [Hannah & Kontar \(2012, 2013\)](#), we use the output of publicly avail-

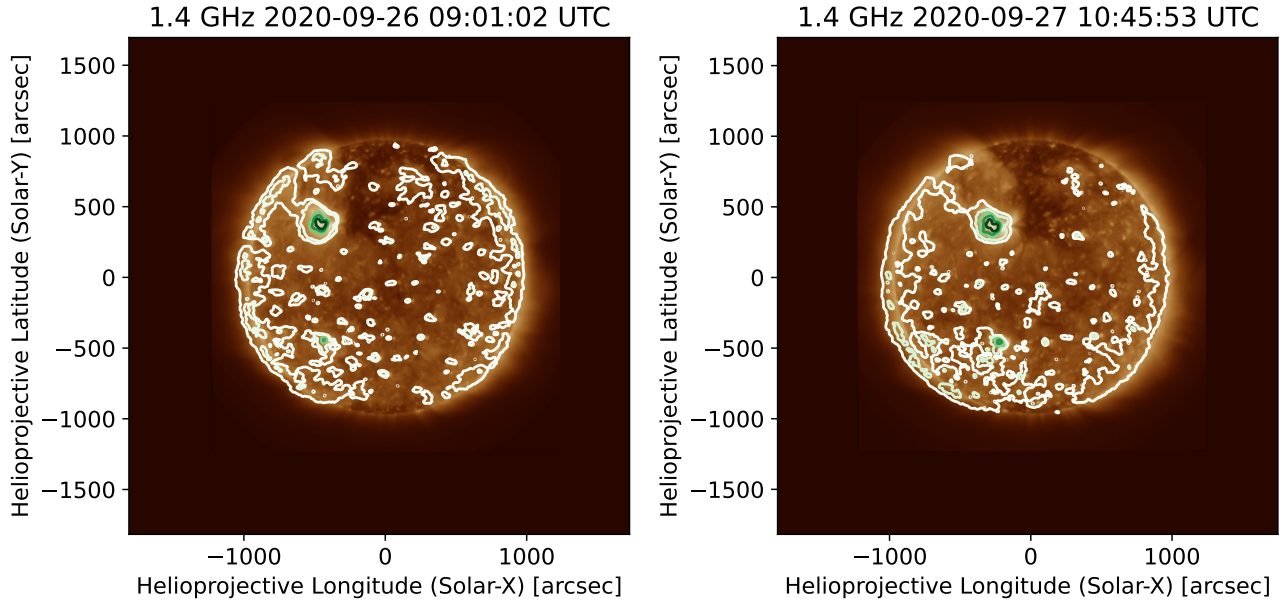


**Figure 6. MeerKAT solar images overlaid on AIA/SDO 193Å images.** **Left panel:** Image for 2020 September 26, 09:07 UTC. Contours are at 4, 10, 40, 60 and 80% of the peak flux density. **Right panel:** Image for 2020 September 27, 10:45 UTC. Contours are at 7, 20, 40, 60 and 80% of the peak flux density. In both images, there are no noise peak at the lowest contour level over a region  $\sim 1 \text{ deg} \times 1 \text{ deg}$ . Lowest contours in both images are chosen at  $20\sigma$  level, where  $\sigma$  is measured rms close to the Sun.

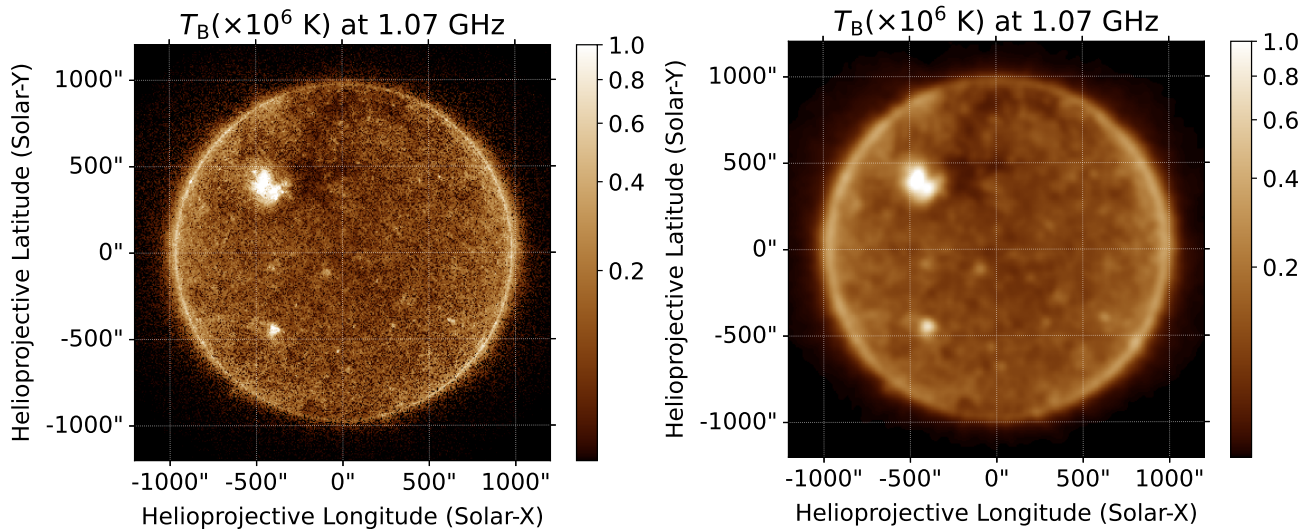


**Figure 7. Simulated radio map and spectrum on 2020 September 26, 09:06 UTC.** **Left panel:** Simulated radio map of the Sun at 1.07 GHz at pixel scale of 2 arcsec. **Right panel:** Same image is convolved with the point-spread-function (PSF) of the observation at 1 GHz (8arcsec).

able code<sup>3</sup> to compute the expected free-free emission using the code developed by [Fleishman et al. \(2021\)](#). A uniform line-of-sight depth of 100 Mm is assumed all through the image. A chromospheric contribution has

been included, assuming that it is proportional to observations at 304Å. The proportionality constant is determined assuming that the chromospheric contribution to the total brightness temperature ( $T_B$ ) is 10880 K ([Zirin et al. 1991](#)). The left panel of Figure 7 shows the simulated  $T_B$  map of the Sun and the right panel shows the same map convolved to the MeerKAT angular res-

<sup>3</sup> <https://github.com/ianan/demreg/tree/master/python>

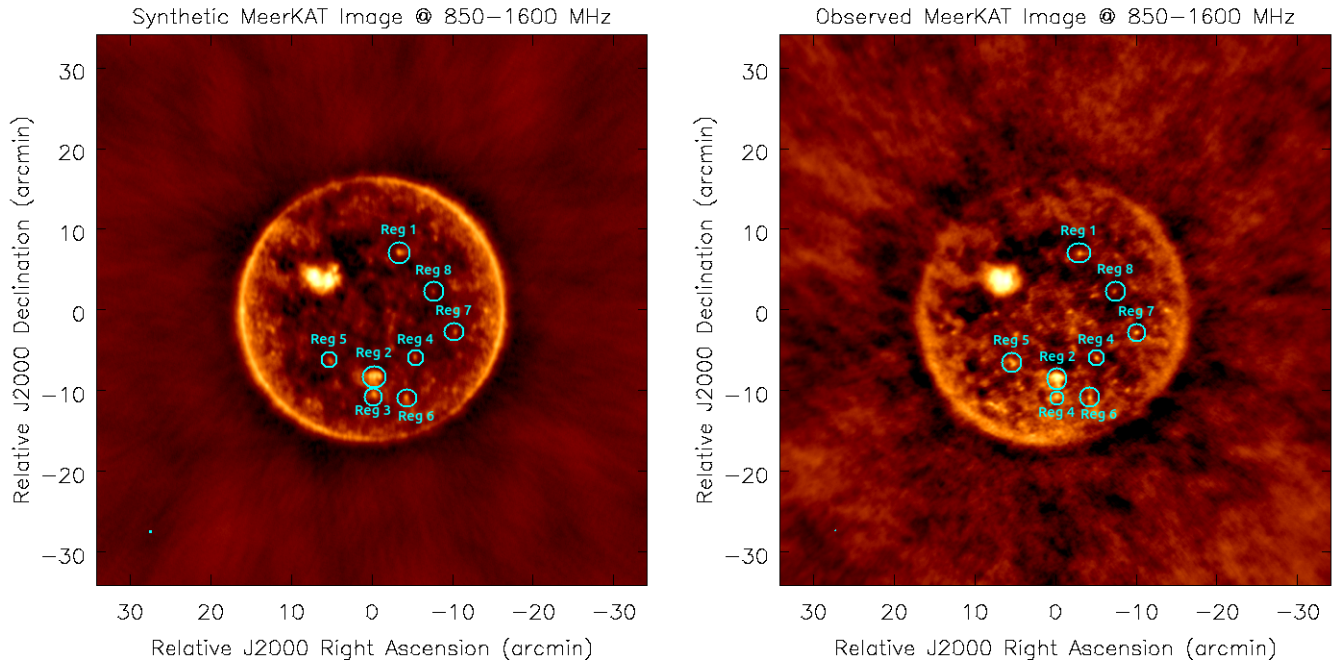


**Figure 8. Comparison between synthetic and observed MeerKAT radio images on 2020 September 27, 10:45 UTC.** **Left panel:** Simulated synthetic solar radio image. **Right panel:** Observed MeerKAT solar radio image. Both images are made using the entire frequency range from 850 – 1600 MHz. In both the images multiple active region bright points have been detected. Some of them are marked by cyan circles.

olution. It is evident from these figures that there are emission at a range of angular scales all the way from instrumental resolution to the size of the solar disc. We note that the simulation does not incorporate any propagation effects like scattering or refraction. While their importance is well established, taking these into account appropriately is beyond the scope of this work.

#### 4.3. Comparing Simulated MeerKAT Images and Observations

Radio interferometry is a Fourier imaging technique, where each baseline of the interferometer measures one Fourier component of the radio sky. Hence, the quality of the images and the scales of emission captured rely crucially on the sampling of the Fourier plane achieved by the interferometric observations. In order to build the appropriate simulated image for comparison with the observed MeerKAT images, we first create simulated visibilities from the simulated images using MeerKAT array configuration and observing parameters used for these observations. These visibilities are then inverted to make the ideal simulated image which would have been observed by MeerKAT. A comparison between simulated MeerKAT image thus obtained and the observed MeerKAT image at the same time is shown in Figure 8. Left panel shows the simulated MeerKAT map and the right panel shows the observed map from MeerKAT. The similarities between the simulated and observed im-

ages are very evident. The most striking similarities are the locations and intensities of the various bright points, some of them have been marked by cyan circles in both the panels. There are also differences, the prominent ones are the presence of noise in the regions beyond the Sun, the limb being not as bright and well defined in the MeerKAT image as compared to the simulated image and the differences in details of the morphology of the brightest active region. While the first of these can be attributed to the combined effect of the thermal noise associated with the image, the imperfections in the calibration and imaging process, scattering in the solar atmosphere plays a significant role for the others. Using a simplistic description for scattering in the solar atmosphere, Bastian (1994) found that at  $\sim 1$  GHz, one does not expect to detect sources with angular sized  $< 10$  arcsec. So one can justifiably expect the finer features approaching this angular size to be washed out in the MeerKAT map, even though they are larger than the instrumental resolution.

#### 4.4. Comparison of Observed and Simulated Spectra

In this section, we compare observed spectra with the expected spectra from the simulated images. As has been mentioned earlier, during these observations the Sun was in the sidelobes of the highly chromatic primary beam of the MeerKAT. At lower parts of the band ( $< 1300$  MHz), the Sun was in the first side lobe of the

primary beam, while at the higher frequencies it was in the second or higher sidelobes, as evident from Figure 2. For further analysis we have chosen spectral points which satisfy the following two conditions:

1. The Sun should not lie beyond the first side lobe of the primary beam, and the value of the primary beam value towards the Sun should be  $> 0.001$  of the peak.
2. The emission should be detected at a level  $> 5\sigma$ , where  $\sigma$  is the rms noise of the primary beam corrected image measured very close to the Sun.

We have extracted spectra for two bright active regions present on the Sun, which are marked by red and green circles in the top panel of Figure 9. Corresponding spectra from this MeerKAT image are shown by filled circles in the bottom panel of Figure 9. The conditions mentioned above are satisfied only below 1070 MHz and that limits the span of the spectra shown here.

We have extracted spectra of these two regions from the corresponding simulated thermal radio maps (one example is shown in Figure 7), which are shown by solid lines in the left bottom panel of the same figure. It is evident that observed values shown by filled circles in the same figure are significantly different from the simulated values. We note that the simulation describes a rather ideal situation and can differ from observations due to several reasons, including the following:

1. Simulation assumes the thermal free-free emission from the coronal plasma to be only emission mechanism in operation. In reality, however, the emission would be a superposition of the thermal free-free emission and gyrosynchrotron/gyroresonance emission (Nindos 2020).
2. The simulation ignores any propagation effects, while in reality refraction and scattering can lead to discernible effects.
3. Interferometers are sensitive only to variations in the brightness distributions and not to a constant background. This implies that interferometers have a tendency to not be sensitive to emissions at large angular scales. The details of the largest angular scale to which an array is sensitive depends upon the details of the array configuration and the sampling of the Fourier domain achieved by the observation under study. This can lead to a reduction in the observed flux density when compared to simulated values.

It is eminently feasible to isolate the impact of the last possibility mentioned above. To do this, we sampled

the simulated map of the Sun using exactly the same Fourier sampling as achieved by the MeerKAT observations and then Fourier inverted it to generate a synthetic simulated map which can be compared directly with the MeerKAT solar maps for an apples-to-apples comparison. The spectra from these synthetic simulated maps are shown by unfilled diamonds in the left panel of Figure 8. The spectra from synthetic simulated maps are consistent with those from the observations. This demonstrates that the large discrepancy between the observed and simulated maps is primarily due to the missing flux density in the MeerKAT maps. The ratio of the flux density measured in the simulated synthetic map to that in the simulated map is defined to be missing flux density fraction and is plotted in the right panel of Figure 8. The missing flux density fraction decreases with the decrease in frequency. For a given array layout, one samples increasingly shorter spacings in the  $uv$ -plane with decreasing frequency and missing flux density fraction is expected to drop. The observed variation in the missing flux density fraction show this trend and substantiates this to be cause of the observed differences between the simulated and MeerKAT solar images. As expected, the missing flux fractions for both the regions show similar spectral behavior. While the other two reasons mentioned above could also be contributing to the observed differences, their effects, however, are smaller than the uncertainty on these measurements.

## 5. CONCLUSION AND FUTURE WORK

The Sun is an extremely complicated radio source with emissions at angular scales ranging from few tens of arcseconds to the size of the solar disc at GHz frequencies, as is evident from simulated radio maps shown in Figure 7. Hence to study the solar radio emission at GHz frequencies, one requires a high DR and high-fidelity spectroscopic snapshot imaging of the Sun. Sufficiently dense spectroscopic snapshot  $uv$ -coverage of the MeerKAT allows high DR imaging of the Sun. Solar observation with the MeerKAT is not yet commissioned, and these observations were done keeping the Sun in the sidelobes of the primary beam.

Here, we have presented the first images of the Sun with the MeerKAT. To the best of our knowledge, given the well-behaved spectroscopic snapshot PSF and the precise calibration, the images presented here are perhaps the highest quality spectroscopic snapshot solar images at these frequencies available to date. To demonstrate the capability of MeerKAT in producing very high-fidelity solar images, we have compared the MeerKAT images with the simulated synthetic images designed to sample exactly the same Fourier components

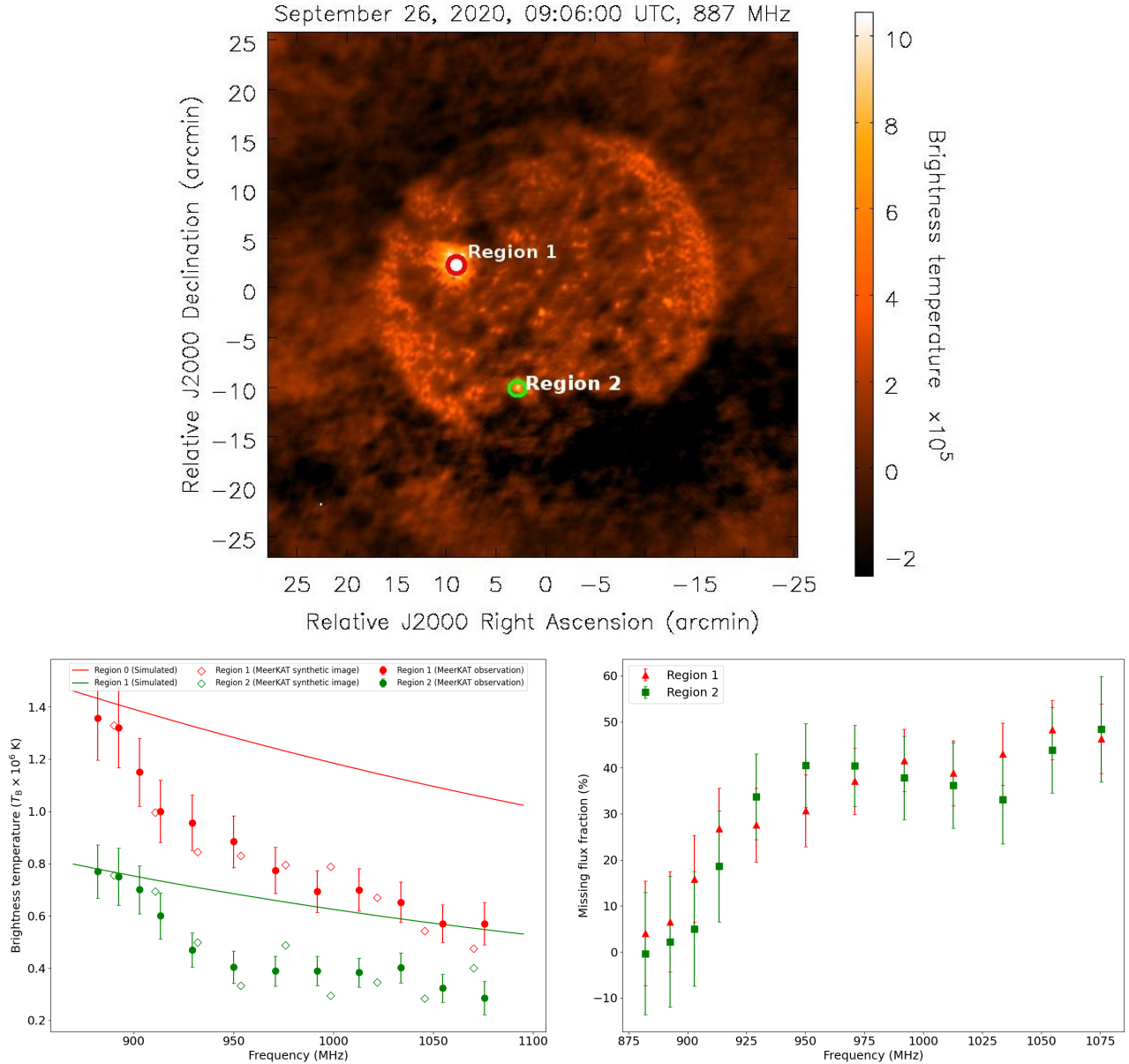


**Figure 9. Comparison of observed spectra with simulated spectra. Top panel:** A sample observed image at 887 MHz. Two regions are marked by red and green circles where spectra have been extracted. Spectra are extracted over a 20arcseconds region centered around these regions. **Bottom left panel:** Spectra for region 1 and 2 are shown by red and green colors, respectively. Solid lines represent the simulated spectra considering thermal emission (One sample image is shown in Figure 7). Unfilled diamonds represent spectra from synthetic MeerKAT map obtained from simulation. Filled circles represent measured spectra from MeerKAT observation on September 26, 2020. **Bottom right panel:** Missing flux fraction is shown as a function of frequency.

as the MeerKAT observations. The correspondence between the observed and simulated images shown in Figure 8 is remarkable and it is evident from that several weak solar emissions present in the synthetic image are detected with high significance in the MeerKAT image.

Although the spatial structures in the observed image match well with the simulated image, from a science perspective, it is also important to test the ability of

MeerKAT for determining the flux densities and spectra of solar features. As substantiated in Section 4.3, the MeerKAT spectra show evidence for missing flux at higher frequencies which drops to insignificant levels by about 900 MHz. An implication is that while the MeerKAT images in the UHF band are not expected to suffer from the missing flux density issue, one will need to be careful about the missing flux density at L band

and higher. A comparison with simulated maps radio maps might provide a good way to quantify the missing flux density fraction for specific observations.

While it is adequate for demonstrating the feasibility of MeerKAT for solar observations and evaluating the quality of the images it can deliver, a key limitation of the present approach arises from the issues related to imaging a source of large angular size in the chromatic primary beam sidelobes. This was however necessitated by the requirement to attenuate the solar signals to a level which would keep the signal chain downstream in its linear regime. A preferable approach for solar observing will be to keep the Sun in the main lobe of the primary beam, and adjust the gains of the appropriate elements of the signal chain to attenuate the signal to the required levels. Some members of this team are currently working with the MeerKAT engineering team to develop a calibration strategy for solar observations along these lines. Once enabled, we are convinced that, with its with its high-fidelity spectroscopic snapshot so-

lar imaging capability, MeerKAT solar observations will open a new frontier in solar radio physics.

The MeerKAT telescope is operated by the South African Radio Astronomy Observatory, which is a facility of the National Research Foundation, an agency of the Department of Science and Innovation. The authors acknowledge the contribution of all those who designed and built the MeerKAT instrument. D.K. and D.O. acknowledge support of the Department of Atomic Energy, Government of India, under the project no. 12-R&D-TFR-5.02-0700. S.M. acknowledges the partial support from USA NSF grant AGS-1654382 to the New Jersey Institute of Technology. This research has also made use of NASA’s Astrophysics Data System (ADS).

*Facilities:* MeerKAT (Jonas & MeerKAT Team 2016; Chen et al. 2021), Solar Dynamics Observatory (SDO; Lemen et al. 2012).

*Software:* astropy (Price-Whelan et al. 2018), matplotlib (Hunter 2007), Numpy (Harris et al. 2020), CASA (McMullin et al. 2007; The CASA Team et al. 2022)

## APPENDIX

Here we discuss in the steps followed for initial flagging, initial calibration, post-calibration flagging and self-calibration.

### A. FLAGGING AND DATA EDITING

On both the epochs, there was no dead antenna. We perform flagging on the 32 K channel data. We have visually examined the data and identify the frequency channels with persistent radio frequency interference (RFI). We first flag any data with zero amplitudes. We then flag the edge channels and all persistent RFI affects spectral channels using `flagdata` task in `CASA`. After that we have performed an automated flagging using `flagdata` in its `tfcrop` mode. Once automated flagging is done, we have extended flags for the time and frequency blocks with more than 80% data are flagged. This initial flagging gives us a comparatively clean fluxcal and phasecal dataset to proceed with the calibration. On the solar scans, we have flagged only the bad frequency channels. Since, solar flux density and spectro-temporal variation is not known a-priori, we did not perform any further automated flagging on the un-calibrated solar scans.

Once initial flagging is done, we averaged eight spectral channels of total width about 200 kHz to reduce the data volume and perform the calibration. We have performed total five rounds of calibration, which are discussed in the following section. After each round of

calibration, we apply the calibration solutions on the fluxcal and phasecal. Each of these calibration rounds is followed by an automated flagging using `tfcrop` and then using `rflag` mode of the `flagdata`. We then extended flags for time and frequencies where more than 80% data have already been flagged. We did the post-calibration flagging on the residual visibilities for the fluxcal and on the corrected visibilities for the phasecal. The post-calibration flagging allowed us to flag any low-level of RFI present in the data and make the next round of calibration solutions less affected due to outliers in the data.

### B. INITIAL CALIBRATION

We performed first two rounds of calibration and post-calibration flagging only on the flux density calibrator, J0408-6545. The model of J0408-6545 is not available in `CASA`. This is brightest source in the field and contribution to the total flux density from other sources in this field is  $\sim 1\%$  at L-band. Hence, we use `CASA` task `setjy` to setup the model of J0408-6545 as described in MeerKAT calibration manual <sup>4</sup>.

We first perform delay calibration using the entire band using the `gaincal` task in `CASA`. Followed by this

<sup>4</sup> J0408-6545 model

a time dependent amplitude-phase calibration is performed on a set of good channels (channel range 1000 to 1100) after applying the delay calibration solutions. We chose a small chunk of channels to ensure that there is no significant frequency dependence while computing the time dependent gain solutions. After that we use both the delay calibration and time-dependent gain solutions, and performed a normalized bandpass calibration over the entire spectral range. Once the bandpass solution is obtained, we use the bandpass solution to correct for frequency dependence and perform a final time-dependent amplitude-phase gain calibration using the full spectral range. We used `solmode=L1R` in `gaincal` task to make the calibration solutions robust in the presence of outliers due to RFI. We call all these steps a single calibration round. Once a single calibration round is finished, we apply delay calibration, bandpass calibration and time-dependent gain calibration solutions using the full spectral range on the calibrator corresponding scans. Each round of calibration is followed by post-calibration flagging as described in Section A.

After two rounds of calibration on the flux density calibrator, we apply the delay and bandpass calibration solutions on the phase calibrator. Then we perform time-dependent gain solution on the phase calibrator assuming a point source model with 1 Jy flux density at the phase center. To scale the gain amplitudes to match the flux density of the phase calibrator, we use CASA task `fluxscale` and obtain the scaled version of the time-dependent gain solutions. We apply these time-dependent gain solutions on the phase calibrator scans followed by post-calibration flagging. We have found that after five rounds of calibration, the residual visibilities for both flux calibrator and phase calibrator look noise like and no noticeable RFI is present on the data.

We apply these final delay, bandpass and time-dependent gain solutions obtained from flux and phase calibrators of the solar scans using the CASA task `applycal` linearly interpolated across time. Since in different scans, Sun is present at different positions of the sky, we treat each 15 minutes solar scans separately for self-calibration and imaging. We also did not consider the full spectral range together, because solar flux density varies with frequency and also the sidelobe response of the primary beam varies significantly with frequency. Hence, after applying the initial calibration solutions obtained towards the phase center, we have splited each solar scans into 20 MHz spectral chunks for self-calibration and imaging.

### C. SELF-CALIBRATION

Although the Sun is at the sidelobes of the primary beam, it is still the source with the highest flux density contributing to the observed visibilities. Before primary beam correction, the brightest source in the field has flux density of 38 mJy/beam, while the peak flux density on the Sun is about 1.7 Jy/beam. Total integrated flux density of background sources is 0.5 Jy, where the integrated flux density of the Sun is about 15 Jy. Since the total contribution from background sources is about 3.3%, they will not affect the self-calibration.

Since the Sun is present about  $2.5^\circ$  away from the phase center, gain solutions towards the phase center may not valid towards the Sun. To tackle the direction-dependent effect, we shifted the phase center of the visibilities to the center of the Sun for each solar scans. We split the each solar scans into 20 MHz spectral chunks and self-calibration is performed for each spectral chunks for each scans separately. This has been done to account for the chromatic primary beam response and spectral dependence of solar structures.

Another major challenge in self-calibrating the solar observation is its flux distribution with baselines. Assuming the Sun as a uniformly illuminated disc of size 32 arcmin, the first ring of the visibility amplitude distribution will lie close to  $100\lambda$  and the visibilities lie less than  $100\lambda$  increases dramatically. Hence one needs good  $uv$ -coverage at these baseline lengths to properly model the emission. But, at present, there are a limited numbers of short baselines  $\leq 100\lambda$  at the MeerKAT, which may cause deconvolution artifacts at longer emission scales. To avoid any deconvolution artifacts due to sparse  $uv$ -coverage at  $\leq 100\lambda$ , we use baselines  $> 100\lambda$  during the self-calibration.

We follow the following self-calibration steps:

1. First we make a circular mask of diameter 34 arcmin centered on the Sun.
2. An image is made using `WSClean` from the data calibrated using `fluxcal` and `phasecal` gain solutions using baselines  $> 100\lambda$ . We use `briggs` weighting<sup>5</sup> with robustness 0. We used a circular taper at  $19k\lambda$ .
3. We kept  $w$ -stacking on in and numbers of  $w$ -plane is chosen automatically by `WSClean`.
4. Deconvolution is performed using the mask centered on the Sun. Average rms ( $\sigma$ ) close to the

<sup>5</sup> Definition of robustness parameter in `WSClean`

Sun is about 0.1 Jy. Hence, we performed deconvolution down to  $3\sigma$ , 0.3 Jy. We used multiscale deconvolution with Gaussian scale sizes 0, 5, 9, 15, 25 and 35 times the pixel size, where one pixel is chosen to 1 arcsec.

5. Deconvolved model of the Sun is converted into model visibilities by WSClean and used for self-calibration.
6. We performed four rounds of phase-only self-calibration and five rounds of amplitude-phase self-calibration. Time-dependent gain solutions are calculated using CASA task `gaincal` at 1 minute time interval using `solmode=L1R` and `minsnr=3` using baselines  $> 100\lambda$ .
7. Due to sidelobe response, visibility amplitudes for two parallel-hand polarizations ( $XX$  and  $YY$ ) could be different. Hence, during the amplitude-phase self-calibration, we make separate sky models for  $XX$  and  $YY$  polarizations.

8. Since some long baseline antennas do not have sufficient signal-to-noise ratio for performing self-calibration, some of them are flagged. Hence, a time-dependent gain solutions are applied using `applycal` task of CASA in `calonly` mode to keep the long baseline antenna with initial calibration solutions.

We have calculated the dynamic range (DR) of the image as the ratio of peak solar flux density and the measured rms close to the Sun. Changes in DR with self-calibration iterations is shown Figure 4. We noticed there is jump in DR when amplitude-phase self-calibration has been initiated, but not a dramatic improvement is observed. Although, we did not see any significant change in DR with self-calibration iterations, it is evident from final images shown in Figure 5 and 3.2 that, there is no significant deconvolution artifacts, which makes these images of having high-fidelity.

## REFERENCES

- Bastian, T. S. 1994, *ApJ*, 426, 774, doi: [10.1086/174114](https://doi.org/10.1086/174114)
- Briand, C., Cecconi, B., Chrysaphi, N., et al. 2022, *URSI Radio Science Letters*, 4, doi: [10.46620/22-0017](https://doi.org/10.46620/22-0017)
- Chen, W., Barr, E., Karuppusamy, R., Kramer, M., & Stappers, B. 2021, *Journal of Astronomical Instrumentation*, 10, 2150013, doi: [10.1142/S2251171721500136](https://doi.org/10.1142/S2251171721500136)
- de Villiers, M. S. 2023, *Astronomical Journal*, 165, 78, doi: [10.3847/1538-3881/acabc3](https://doi.org/10.3847/1538-3881/acabc3)
- de Villiers, M. S., & Cotton, W. D. 2022, *The Astronomical Journal*, 163, 135, doi: [10.3847/1538-3881/ac460a](https://doi.org/10.3847/1538-3881/ac460a)
- Fleishman, G. D., Kuznetsov, A. A., & Landi, E. 2021, *The Astrophysical Journal*, 914, 52, doi: [10.3847/1538-4357/abf92c](https://doi.org/10.3847/1538-4357/abf92c)
- Fox, N. J. 2017, in *AGU Fall Meeting Abstracts*, Vol. 2017, SH21C-02
- García Marirrodriga, C., Pacros, A., Strandmoe, S., et al. 2021, *A&A*, 646, A121, doi: [10.1051/0004-6361/202038519](https://doi.org/10.1051/0004-6361/202038519)
- Gary, D. E., Nita, G. M., & Sane, N. 2012, in *American Astronomical Society Meeting Abstracts*, Vol. 220, American Astronomical Society Meeting Abstracts #220, 204.30
- Hallinan, G., Anderson, M., Isella, A., et al. 2023, in *American Astronomical Society Meeting Abstracts*, Vol. 55, American Astronomical Society Meeting Abstracts, 451.09
- Hannah, I. G., & Kontar, E. P. 2012, *A&A*, 539, A146, doi: [10.1051/0004-6361/201117576](https://doi.org/10.1051/0004-6361/201117576)
- . 2013, *A&A*, 553, A10, doi: [10.1051/0004-6361/201219727](https://doi.org/10.1051/0004-6361/201219727)
- Harris, C. R., Millman, K. J., van der Walt, S. J., et al. 2020, *Nature*, 585, 357, doi: [10.1038/s41586-020-2649-2](https://doi.org/10.1038/s41586-020-2649-2)
- Heywood, I., Rammala, I., Camilo, F., et al. 2022, *The Astrophysical Journal*, 925, 165, doi: [10.3847/1538-4357/ac449a](https://doi.org/10.3847/1538-4357/ac449a)
- Hunter, J. D. 2007, *Computing in Science & Engineering*, 9, 90, doi: [10.1109/MCSE.2007.55](https://doi.org/10.1109/MCSE.2007.55)
- Jonas, J., & MeerKAT Team. 2016, in *MeerKAT Science: On the Pathway to the SKA*, 1, doi: [10.22323/1.277.0001](https://doi.org/10.22323/1.277.0001)
- Kansabanik, D. 2022, *Solar Physics*, 297, 122, doi: [10.1007/s11207-022-02053-x](https://doi.org/10.1007/s11207-022-02053-x)
- Lemen, J. R., Title, A. M., Akin, D. J., et al. 2012, *SoPh*, 275, 17, doi: [10.1007/s11207-011-9776-8](https://doi.org/10.1007/s11207-011-9776-8)
- Lonsdale, C. J., Cappallo, R. J., Morales, M. F., et al. 2009, *IEEE Proceedings*, 97, 1497, doi: [10.1109/JPROC.2009.2017564](https://doi.org/10.1109/JPROC.2009.2017564)
- McMullin, J. P., Waters, B., Schiebel, D., Young, W., & Golap, K. 2007, in *Astronomical Society of the Pacific Conference Series*, Vol. 376, *Astronomical Data Analysis Software and Systems XVI*, ed. R. A. Shaw, F. Hill, & D. J. Bell, 127

- Mondal, S., Mohan, A., Oberoi, D., et al. 2019, *The Astrophysical Journal*, 875, 97, doi: [10.3847/1538-4357/ab0a01](https://doi.org/10.3847/1538-4357/ab0a01)
- Müller, D., St. Cyr, O. C., Zouganelis, I., et al. 2020, *A&A*, 642, A1, doi: [10.1051/0004-6361/202038467](https://doi.org/10.1051/0004-6361/202038467)
- Nindos, A. 2020, *Frontiers in Astronomy and Space Sciences*, 7, 57, doi: [10.3389/fspas.2020.00057](https://doi.org/10.3389/fspas.2020.00057)
- Offringa, A. R., McKinley, B., Hurley-Walker, N., et al. 2014, *Monthly Notices of the Royal Astronomical Society*, 444, 606, doi: [10.1093/mnras/stu1368](https://doi.org/10.1093/mnras/stu1368)
- Price-Whelan, A. M., Sipőcz, B., Günther, H., et al. 2018, *The Astronomical Journal*, 156, 123
- Raouafi, N. E., Matteini, L., Squire, J., et al. 2023, *Space Science Reviews*, 219, 8, doi: [10.1007/s11214-023-00952-4](https://doi.org/10.1007/s11214-023-00952-4)
- Rast, M. P., Bello González, N., Bellot Rubio, L., et al. 2021, *Solar Physics*, 296, 70, doi: [10.1007/s11207-021-01789-2](https://doi.org/10.1007/s11207-021-01789-2)
- Reber, G. 1944, *ApJ*, 100, 279, doi: [10.1086/144668](https://doi.org/10.1086/144668)
- Rimmele, T. R., Warner, M., Keil, S. L., et al. 2020, *SoPh*, 295, 172, doi: [10.1007/s11207-020-01736-7](https://doi.org/10.1007/s11207-020-01736-7)
- The CASA Team, Bean, B., Bhatnagar, S., et al. 2022, *Publications of the Astronomical Society of the Pacific*, 134, 114501, doi: [10.1088/1538-3873/ac9642](https://doi.org/10.1088/1538-3873/ac9642)
- Tingay, S. J., Goeke, R., Bowman, J. D., et al. 2013, *Publications of the Astronomical Society of Australia*, 30, e007, doi: [10.1017/pasa.2012.007](https://doi.org/10.1017/pasa.2012.007)
- van Haarlem, M. P., Wise, M. W., Gunst, A. W., et al. 2013, *Astronomy and Astrophysics*, 556, A2, doi: [10.1051/0004-6361/201220873](https://doi.org/10.1051/0004-6361/201220873)
- Wayth, R. B., Tingay, S. J., Trott, C. M., et al. 2018, *Publications of the Astronomical Society of Australia*, 35, e033, doi: [10.1017/pasa.2018.37](https://doi.org/10.1017/pasa.2018.37)
- Zarka, P., Coffre, A., Denis, L., et al. 2018, in 2018 2nd URSI Atlantic Radio Science Meeting (AT-RASC), 1–1, doi: [10.23919/URSI-AT-RASC.2018.8471648](https://doi.org/10.23919/URSI-AT-RASC.2018.8471648)
- Zirin, H., Baumert, B. M., & Hurford, G. J. 1991, *ApJ*, 370, 779, doi: [10.1086/169861](https://doi.org/10.1086/169861)